Results in Optics 13 (2023) 100575

Contents lists available at ScienceDirect

Results in Optics

journal homepage: www.sciencedirect.com/journal/results-in-optics

Highly compact tunable hourglass-shaped graphene band-stop filter at terahertz frequencies

Ghader Mohammadi, Aliasghar Orouji, Mohammad Danaie *

Faculty of Electrical and Computer Engineering, Semnan University, Semnan, Iran

ARTICLE INFO

Keywords:
Band-rejection filter
Chemical potential
Graphene
Plasmonic
Surface plasmon
Terahertz

ABSTRACT

In this research paper, we introduce a band-stop filter based on an hourglass-shaped graphene nanoribbon topology. Employing the three-dimensional finite difference time domain (3D-FDTD) method, we conduct comprehensive numerical simulations to investigate transmission spectra and electromagnetic field distributions. Our primary objectives are to achieve high transmission efficiency, increase tunability, and ensure compact dimensions. The hourglass-shaped band-stop filter exhibits a remarkable bandwidth of 1.2 THz, a 90 % transmission efficiency in the passband, an impressive attenuation of −52.5 dB at the resonance frequency of 32.3 THz, and a compact footprint of 400×300 nm^2. By manipulating the chemical potential (or bias voltage) to control the conductivity and dielectric constant of the graphene surface, we set the center frequency of the filter in the range of 28 to 36 terahertz. The remarkable combination of high transmission efficiency, high tunability, and compact design makes our proposed filter an ideal candidate for integration.

1. Introduction

Graphene, an atom-thick two-dimensional structure with carbon atoms arranged in a honeycomb lattice, finds numerous applications in photonics and optoelectronics within the terahertz frequency range (Youngblood et al., 2014). With its complex permittivity, graphene has emerged as a unique material, boasting extraordinary properties such as exceptional electrical and thermal conductivity, high charge carrier density and mobility, reduced losses, resonance mode confinement, broad and high-speed performance, and remarkable optical conductivity (Farbod et al., 2022; Yao, 2013; Gómez-Díaz and Perruisseau-Carrier, 2013; Xiang et al., 2014). Doped graphene, akin to metals, supports surface plasmon polariton (SPP) modes beyond the mid-infrared region, enabling the confinement of electromagnetic waves at sub-wavelength scales and overcoming the limitations of light diffraction (Li et al., 2014; Zhao et al., 2014; Gao et al., 2014; Li et al., 2016). Consequently, the excellent properties of graphene have garnered significant attention from researchers (Li et al., 2014; Shiramin and Van Thourhout, 2016). Table 1.

A prominent characteristic of graphene lies in its ability to alter the chemical potential or Fermi energy through external voltage application, leading to changes in conductivity and central frequency (Liu et al., 2017; Shi et al., 2016; Xiao et al., 2017). Different chemical potentials yield varying optoelectronic properties in graphene (Liu et al., 2017; Chen et al., 2017). Comparatively, graphene offers distinct advantages over noble metals like gold and silver: its plasmon wavelength is much shorter, resulting in a strong wave concentration edge of the graphene due to these short wavelengths and large propagation constants (Christensen et al., 2012b; Shafagh et al., 2021). Moreover, graphene exhibits lower losses compared to noble metals (Chorsi and Gedney, 2016; Wei et al., 2016). As a result of these benefits, graphene-based devices have witnessed remarkable progress in recent years, including modulators (Liu et al., 2016; Mohsin et al., 2016; Nouman et al., 2016), band-stop filters (Melo et al., 2022; Wang et al., 2018), photodetectors (Gosciniak et al., 2020; Ryzhii et al., 2020), heaters (Vertuccio et al., 2019), waveguides (Li et al., 2022; Xing et al., 2018), transistors (Danielson et al., 2020; Ganguli et al., 2020), switches (Hu et al., 2021; Hu and Wang, 2017; Zhou and Song, 2022), absorbers (Nickpay et al., 2023a; Nickpay et al., 2023b; Nickpay et al., 2022); antennas (Chashmi et al., 2019; Chashmi et al., 2020) and sensors (Snapp et al., 2019; Mansouri et al., 2023). Among the various devices available, optical filters based on graphene find extensive applications in optical receivers and telecommunications (Romagnoli, 2018; Kuscu et al., 2021; Li et al., 2013).

One of the most fascinating features of graphene is that it can replace metals in plasmonic devices. Plasmonic devices based on metals suffer

* Corresponding author.
E-mail addresses: ghader.mohammadi@semnan.ac.ir (G. Mohammadi), aliaorouji@semnan.ac.ir (A. Orouji), danaie@semnan.ac.ir (M. Danaie).

https://doi.org/10.1016/j.rio.2023.100575
Received 21 September 2023; Received in revised form 20 October 2023; Accepted 23 October 2023
Available online 27 October 2023

from high energy losses due to ohmic losses (Hajshahvaladi et al., 2022a; Danaie and Geravand, 2018; Khani et al., 2020a; Khani et al., 2020b; Moradi et al., 2022; Jafari et al., 2021). Graphene, on the other hand, has exceptionally low intrinsic losses in the infrared and terahertz ranges, making it more efficient for plasmonic applications. Furthermore, it can be integrated with other 2D materials or heterostructures, allowing for the creation of complex and multifunctional plasmonic devices with tailored properties. Finally, graphene-based plasmonic devices are thinner and more compact than their metal or photonic crystal counterparts (Hajshahvaladi et al., 2022b; Danaie et al., 2023; Nohoji and Danaie, 2022; Danaee et al., 2019; Yousefi and Maleki, 2023). This is especially useful for miniaturization and flexible or wearable applications.

Band-pass and band-stop filters are particularly widely used filter types. In the existing literature, various graphene filters have been investigated. In the past few years, several researchers have proposed different designs for band-stop filters using graphene waveguides and cavities. For instance, in 2017, Ze-Jiang and Jiu-Sheng introduced a band-stop filter comprising one graphene waveguide and four cavities, with a central frequency of 6 THz. This design achieved a high-Q band-rejection terahertz wave filter with an efficiency of 1500 (Ze-Jiang and Jiu-Sheng, 2018). Following that, in 2018, Dongwei Zhai et al. presented another band-stop filter with a wide range of center wavelengths (CWLs) from 2.0 THz to 0.5 THz. Their design boasted high selectivity, and the transmission spectrum exhibited minimal attenuation at the cut-off frequency (-3dB) (Zhai et al., 2018). In 2019, Morteza Janfaza et al. suggested a band-stop and narrow band-pass filter-based on defected Bragg gratings. Although their design offered suitable frequency selection, the transmission spectrum demonstrated lower efficiency in the band pass (Janfaza et al., 2019). Building upon these previous studies, in 2022, Meiping Li et al. introduced a band-stop filter with switchable single/double plasmon-induced transparency, utilizing a metal-dielectric-metal waveguide. Their filter design allowed for the adjustable frequency with changes in chemical potentials, but it did require relatively larger dimensions (Li et al., 2022). More recently, in 2023, Seyed Abed Zonouri et al. proposed a new band-stop filter using graphene hook-shaped resonators for the terahertz region. This design exhibited a high-quality factor of 22.5 % and a dual-band feature, with the transmission spectrum showing no significant attenuation at the cut-off frequency (Zonouri and Hayati, 2023).

Despite these advancements, one of the challenges for graphene band-stop filters remains in designing an adjustable filter with high transmission efficiency while maintaining compact dimensions suitable for integrated optical telecommunications devices (Gonçalves and Peres, 2016). In this context, we presented a novel graphene band-stop filter with an hourglass-shaped nanoribbon. The filter appears to have high transmission efficiency, excellent tunability, and compact dimensions, making it a promising candidate for integrated optical telecommunication applications.

2. Numerical analysis of the graphene model

Surface plasmon polaritons (SPPs) are a form of electromagnetic waves that propagate along the boundary between a dielectric material and a metal or graphene. SPPs have garnered significant interest due to their remarkable attributes, including their ability to surpass the refractive limitations and their capacity to control light on a sub-wavelength level. As a result, they stand as promising contenders for the development of extensively integrated optical circuits (Khani et al., 2021; Krishnamoorthy et al., 2022; Korani et al., 2023). The propagation of electromagnetic waves on a graphene sheet placed over a dielectric substrate, which supports SPP wave propagation modes, can be analyzed using the dispersion equation (Gonçalves and Peres, 2016).

$$\beta = \frac{2i\omega\varepsilon_{eff}\varepsilon_0}{\sigma_g} \tag{1}$$

The SPP propagation constant (β) in this equation is influenced by various parameters, including the angular frequency (ω), the permittivity of vacuum (ε_0), and ε_{eff} is the effective permittivity constant of the surrounding medium, which is obtained using Eq. (2) (Cai et al., 2018; Sepahvandi et al., 2023).

$$\varepsilon_{eff} = \varepsilon_0 + i\frac{\sigma_g}{H\omega} \tag{2}$$

The effective permittivity involves the thickness of graphene (H) and the optical surface conductivity of graphene (σ_g), which is obtained through the Kubo formula (Xing et al., 2018; Huang et al., 2022; Heydari, 2022). The surface optical conductivity of single-layer graphene is influenced by interband and intraband transitions, leading to the division of optical surface conductivity into inter-band and intra-band terms (Heydari, 2022; Naghdehforushha and Moradi, 2019).

$$\sigma_g(\omega.\mu.\Gamma.T) = \sigma_{intera} + \sigma_{inter} \tag{3}$$

$$\sigma_{intera} = 2\frac{e^2 K_B T}{\pi\hbar^2}\cdot\frac{i}{\omega + i\,\tau^{-1}}\left[\ln\left[2\cosh\left(\frac{\mu_c}{K_B T}\right)\right]\right] \tag{4}$$

$$\sigma_{inter} = \frac{e^2}{4\hbar}\left[\frac{sinh\left(\frac{\hbar\omega}{2TK_B}\right)}{cosh\left(\frac{\hbar\omega}{2TK_B}\right) + cosh\left(\frac{\mu_c}{TK_B}\right)} - \frac{i}{\pi 2}ln\frac{(\hbar\omega + 2\mu_c)^2}{(\hbar\omega - 2\mu_c)^2 + (2TK_B)^2}\right] \tag{5}$$

where $\hbar = h/2\pi$ is the reduced Planck constant, $k_B = 1.38064852\times10^{-23}\ \frac{m^2 kg}{s^2 k}$, is the Boltzmann constant, T is the temperature, $e = 1.60217662\times10^{-19}$ C is the charge of the electron, μ_c is the chemical potential of the graphene sheet, $\Gamma = \tau^{-1}$ is the scattering rate(eV), and τ is the relaxation time (Hu and Wang, 2017; Huang et al., 2022; Shi et al., 2016; Wang et al., 2012; Zhuang et al., 2016). In the mid-infrared region, and at room temperature (T = 300 K), Kubo's equation is reduced to equation (6), which is similar to Drud's equation (Cai et al., 2018; Wang et al., 2018; Xiao et al., 2018).

$$\sigma_g = \frac{ie^2\mu_c}{\pi\hbar^2(\omega + i\tau^{-1})} \tag{6}$$

To calculate the real and imaginary parts of the mono-layer graphene sheet conductivity in the range of 1–50 THz, we utilized the finite-difference time-domain (FDTD) method. Setting the scattering rate, chemical potential, and temperature to specific values (0.00011 eV, 0.5 eV, and 300 K, respectively) (Tavana et al., 2022). We obtained accurate results, as illustrated in Fig. 1. Where the curve of the analytic data closely aligns with the values used in our FDTD model.

3. Design of graphene-based band-stop filter

The optical conductivity of graphene exhibits a strong frequency dependence (Khani et al., 2020a). The main performance of the band-stop filter is primarily influenced by the incidence of high-frequency waves at the structure's input, leading to the excitation of graphene's

Table 1
Band-stop filter specifications in the most optimal conditions.

Resonance frequency	Chemical potential	Waveguide length	Nanoribbon width	Nanoribbon height	Bandwidth filter
32.3 THz	0.5–0.3 eV	320 nm	50 nm	150 nm	1.2 THz

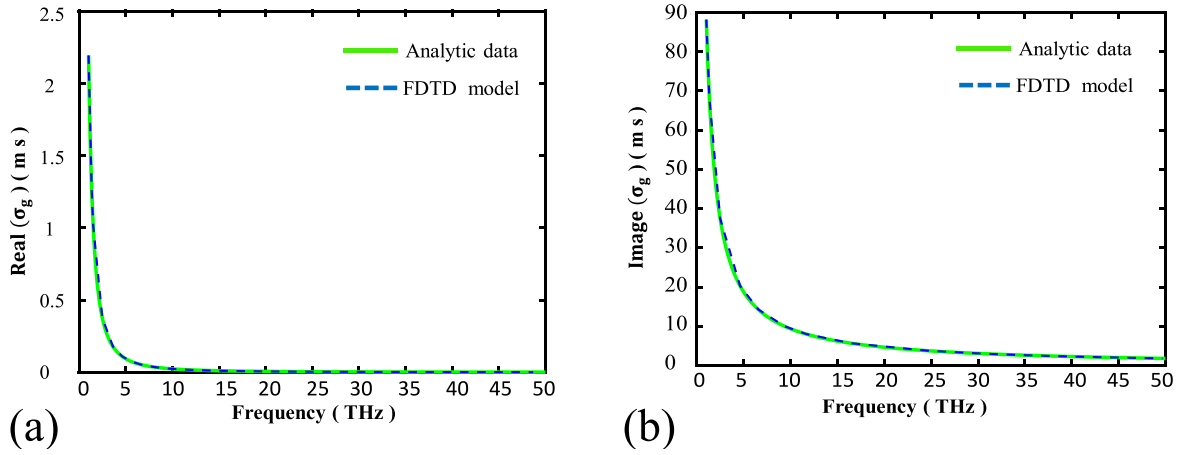

Fig. 1. (a) The real versus (b) imaginary parts surface conductivity of graphene varies from 0 to 50 THz.

surface plasmon polariton (SPP) (Liu et al., 2016). Fig. 2. shows both the 2D and 3D views of the proposed tunable band-stop filter, which comprises a graphene waveguide and an hourglass-shaped graphene ribbon placed on a substrate with a dielectric constant of $\varepsilon_r = 4$ (Gómez-Díaz and Perruisseau-Carrier, 2013). The dimensions of the filter structure along the x, y, and z axes are 400 nm, 300 nm, and 200 nm, respectively. The width of the waveguide of the graphene sheet along the y-axis is 150 nm and the width of the middle ribbon is 50 nm (Azar et al., 2018).

In Fig. 3(a), the transmission spectrum with chemical potential for graphene waveguide and graphene strip is obtained at 0.5 and 0.3 electron volts, respectively. The distance between the mode source and the transmission spectrum monitor is 320 nm. For the investigation of properties and simulation of terahertz wave propagation in the band-stop filter, the 3D-FDTD method is employed. Perfectly matched layers (PML) are used for boundary conditions along the x and −x directions, while a symmetric layer is applied along the -y direction. Metal layers are used for +y, −z, and +z directions. The SPP modes are excited along the x-axis on the left side of the filter using a light source mode. To enhance the accuracy of simulation calculations, a mesh size of 2 nm in the x and y directions and 2.5 nm in the z directions was utilized. According to Fig. 3(b), by applying a bias voltage between the graphene surface, and the substrate, we can adjust the density of free carriers, excite the electron-hole pairs, and change the fermi level and intraband losses of graphene, which leads to a change in the chemical potential (according to Eq. (7)) and the surface conductivity of graphene (Gómez-Díaz and Perruisseau-Carrier, 2013).

$$\mu_c = \hbar . \mathrm{Vf} \sqrt{\frac{\pi \varepsilon_0 \varepsilon_r V_{bias}}{e.D_{si}}} \tag{7}$$

In Eq. (7), V_f and D_{si} represent the fermi voltage and the thickness of the Si substrate, respectively. These conditions enable us to modify the frequency of the filter by selecting and altering the shape of the graphene structure and adjusting the bias voltage. The main advantage of this setup is that, following the fabrication process, if necessary, the cut-off frequency of the band-stop filter can be conveniently adjusted by simply changing the bias voltage and chemical potential (Cai et al., 2018).

In graphene-based devices and structures, the chemical potential serves as a variable parameter, influencing the surface conductivity of graphene as per Eq. (6). Consequently, the surface conductivity changes, leading to shifts in the cut-off frequency of the band-stop filter. In Fig. 3 (b), the representation of the filter's transfer curve is presented, demonstrating an adjustable central frequency spanning from 28.2 THz to 36.2 THz. This tuning begins at 28.2 terahertz when μc_1 is established at 0.42 eV and μc_2 at 0.22 eV, as seen in the cyan curve labeled as A.

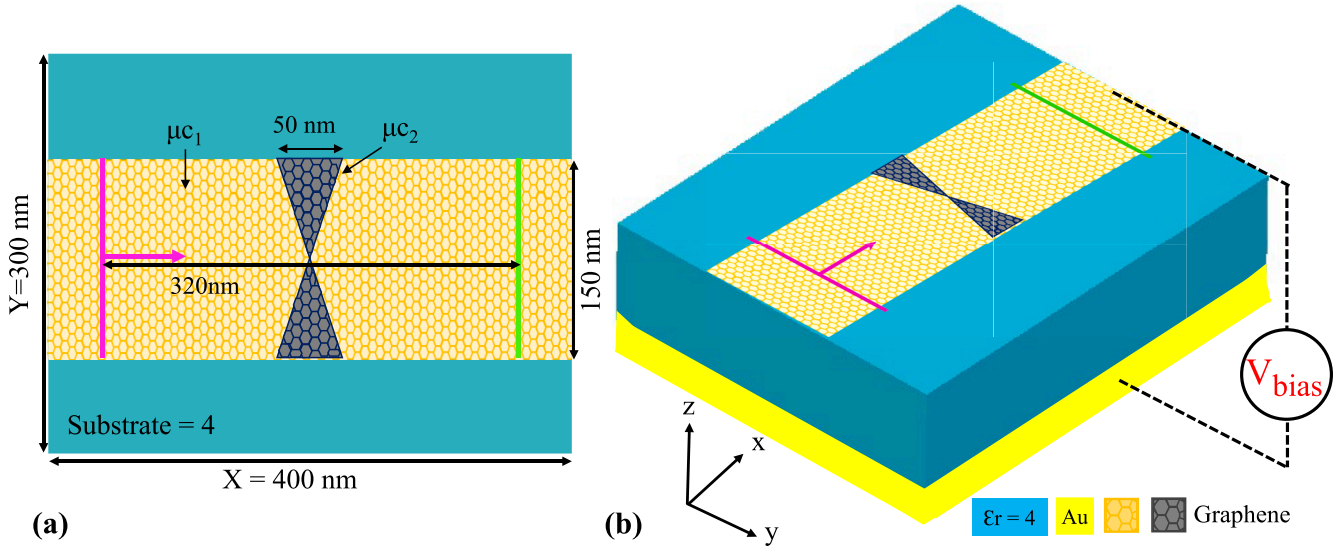

Fig. 2. (a) Characteristics and two-dimensional view of band-step filter with hourglass-shaped graphene strip (b) Three-dimensional schematic of the band-stop filter THz.

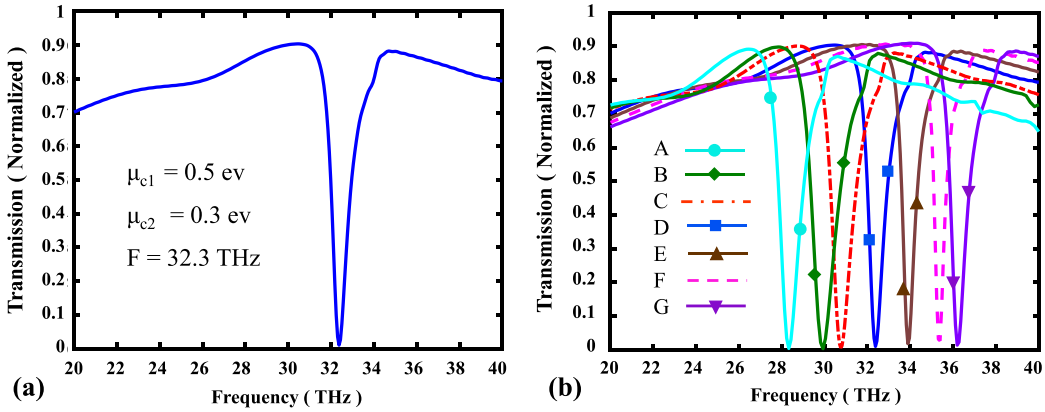

Fig. 3. (a) Transmission spectrum at the cut-off frequency of 32.3 THz (b) Transmission spectrum of the band-stop filter with changes of μc_1 and μc_2.

Further refinements yield a shift in the central frequency to 29.9 THz by assigning μc_1 as 0.44 eV and μc_2 as 0.24 eV, showcased in the green curve designated as B. Similarly, adjusting μc_1 to 0.46 eV and μc_2 to 0.26 eV results in a central frequency of 30.7 THz, indicated by the red curve. Equally, configuring μc_1 to 0.5 eV and μc_2 to 0.3 eV (blue curve D) leads to a central frequency of 32.3 THz, while implementing μc_1 at 0.54 eV and μc_2 at 0.34 eV (brown curve E) results in a central frequency of 33.9 THz. Notably, setting the chemical potentials to μc_1 of 0.58 eV and μc_2 of 0.38 eV (magenta curve F) generates a central frequency of 35.3 THz. Similarly, choosing μc_1 as 0.62 eV and μc^2 as 0.42 eV (violet curve G) achieves the highest central frequency of 36.2 THz. Impressively, the central frequency of the filter can be finely adjusted by manipulating the chemical potential of graphene within the range of 28 to 36 Hz, yielding remarkable outcomes. The most optimal mode demonstrates an attenuation coefficient of −52 dB and a bandwidth of 1.2 THz.

Fig. 4(a and b) illustrates the electric field magnitude distribution at 31 and 32.3 terahertz frequencies, for the bandpass and cutoff regions, respectively. Additionally, in Fig. 4(c and d), we present the electric field distribution (Re ($|E_z|$)), at these same frequencies. As evident, particularly in Fig. 4(a), the field distribution resides along the edge of the waveguide and the graphene ribbon. Notably, the field exhibits a high intensity within the graphene ribbon.

4. Results and discussions

In structures comprising graphene nanoribbons within a graphene waveguide, the dispersion relation governing the propagation of surface plasmons cannot be derived through analytical means. Consequently, numerical full-wave solvers are employed. Two distinct modes of propagation surface plasmon polaritons (SPPs) exist in this context. One mode entail confining the electromagnetic field at the edges of the graphene sheet, while the other involves confining the field along the length of the graphene ribbon (Fig. 4(a)). The extent of field confinement is primarily influenced by the relaxation time of graphene, with minimal impact on the propagation length of these modes. Furthermore, adjusting the chemical potential of graphene provides a means of tuning the properties of these modes (Gómez-Díaz and Perruisseau-Carrier, 2013; Christensen et al., 2012a; Nikitin et al., 2011).

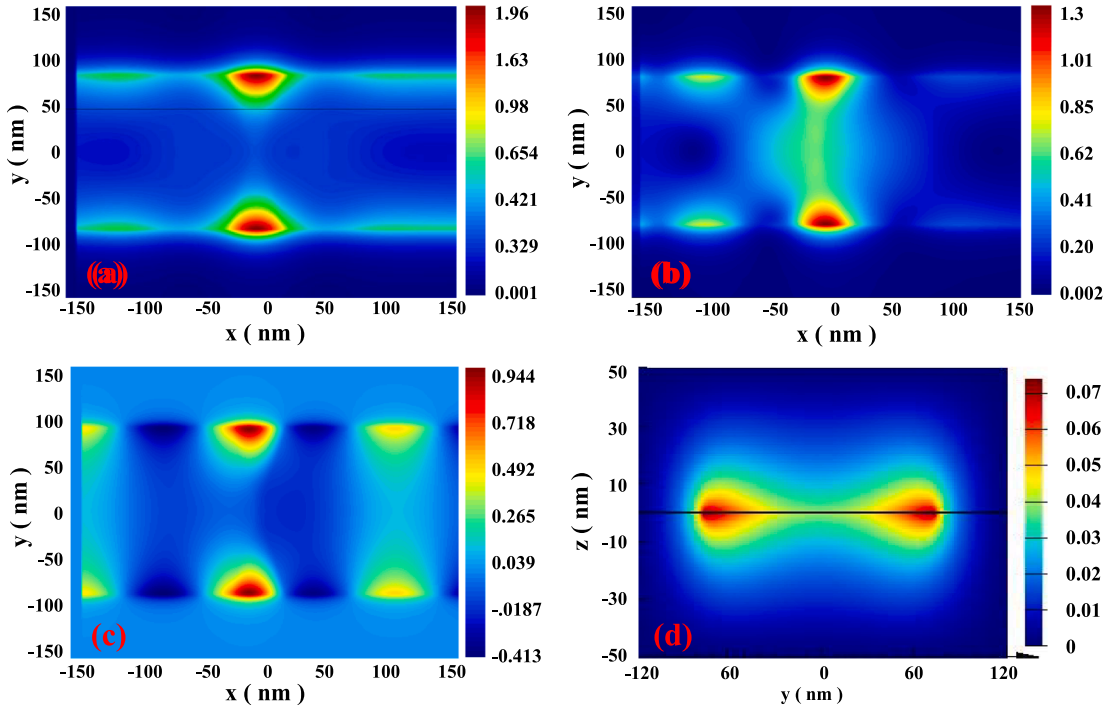

Fig. 4. (a) Magnitude of the field distribution in the passband region (b) Magnitude of the field distribution in the cutoff frequency region (c) Field distribution (Re ($|E_z|$)) in the passband region (d) Field distribution (Re ($|E_x|$)) in the propagation mode.

In Fig. 5, we explore varying heights of nanoribbon graphene. The nanoribbon height of 120 nm leads to a reduction of the transmission spectrum, and further reduction of the nanoribbon height to 100 nm leads to a significant reduction of the transmission spectrum. However, at a nanoribbon height of 150 nm, we observe the most optimal transmission spectrum without any ripple.

In Fig. 6(a), we investigate distinct widths of graphene nanoribbons. Employing a nanoribbon width of 70 nm, a portion of the transmission spectrum displays minor ripple, but approaches the optimal condition. However, at a nanoribbon width of approximately 50 nm, we achieve the highest transmission spectrum devoid of ripple. Using nanoribbon 40 nm, the transmission spectrum is relatively normal, but there is less attenuation at the cutoff frequency compared to the 50 nm nanoribbon.

In Fig. 6(b), we explore various junction widths between the upper and lower segments of the graphene nanoribbon. Employing junction widths of 10 nm, 20 nm, 30 nm, and 40 nm induces a slight reduction in transmission spectrum intensity, accompanied by minor oscillations within the transmission spectrum's bandpass. Remarkably, adopting a 1 nm junction width yields the most favorable outcome, characterized by the highest attainable transmission spectrum without any ripple.

By varying the chemical potential ratio of the band-stop filter, we observe changes in the bandwidth, central frequency, and output efficiency. Fig. 7(a) illustrates the effects of different chemical potential ratios (rμ) on the transition output. For instance, when $r_\mu = 1.66$ ($\mu_{c1} = 0.5$ eV and $\mu_{c2} = 0.3$ eV), the transition output (magenta curve) exhibits a central frequency of 32.4 THz with an attenuation of −19 dB. At $r_\mu = 2.0$ ($\mu_{c1} = 0.6$ eV and $\mu_{c2} = 0.3$ eV), the transition output (red curve) has a central frequency of 33 THz with an attenuation of −21 dB. Similarly, at $r_\mu = 2.33$ ($\mu_{c1} = 0.7$ eV and $\mu_{c2} = 0.3$ eV), the transition output (blue curve) shows a central frequency of 34.4 THz with an attenuation of −26 dB, and at $r_\mu = 2.66$ ($\mu_{c1} = 0.8$ eV and $\mu_{c2} = 0.3$ eV), the transition output (cyan curve) exhibits a central frequency of 36 THz with an attenuation of −35 dB. Fig. 7(b) explores the scenario where the chemical potential of the graphene waveguide (μ_{c1}) is kept constant, while only the chemical potential of the graphene nanoribbon (μ_{c2}) is varied. At $r_\mu = 2.5$ ($\mu_{c1} = 0.5$ eV and $\mu_{c2} = 0.2$ eV), the transition output (magenta curve) features a central frequency of 30.5 THz with an attenuation of −52.5 dB. When rμ = 2.0 ($\mu_{c1} = 0.5$ eV and $\mu_{c2} = 0.25$ eV), the transition output (red curve) exhibits a central frequency of 31.7 THz with an attenuation of −27.5 dB. At $r_\mu = 1.66$ ($\mu_{c1} = 0.5$ eV and $\mu_{c2} = 0.3$ eV), the transition output (blue curve) displays a central frequency of 32.4 THz with an attenuation of −19 dB. Finally, at $r_\mu = 1.43$ ($\mu_{c1} = 0.5$ eV and $\mu_{c2} = 0.35$ eV), the transition output (cyan curve) showcases a central frequency of 33 THz with an attenuation of −12.2 dB. The calculated bandwidth of the band-stop filter is BW = 1.2 THz.

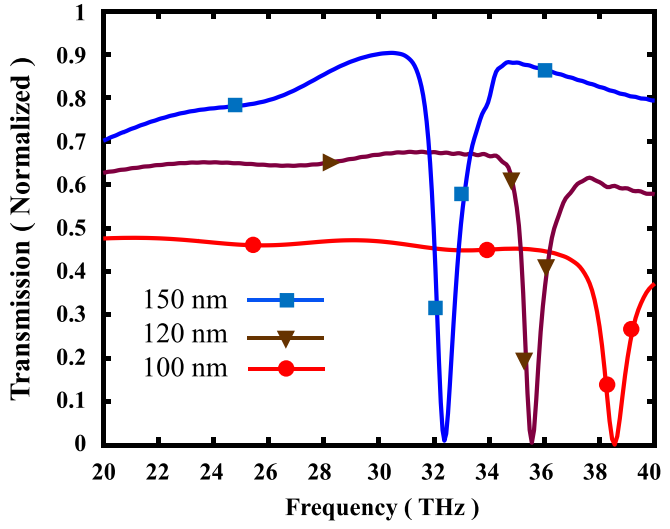

Fig. 5. Transmission spectra for the height of graphene nanoribbons of different sizes.

Table 2 provides a comparison of the presented band-stop filter with various filters reported in recent publications, highlighting different characteristics in the terahertz range. Each graphene band-stop filter with distinct structures exhibits varying bandwidths and frequencies, catering to specific applications and requirements. Notably, the presented filter stands out with its smaller dimensions (nm^2) compared to the other filters listed in Table 2, making it advantageous for integration into optical telecommunication devices.

5. The process of fabrication of graphene nanoribbon

In the field of nanoscale optical devices, obtaining graphene nanoribbons (GNRs) with precisely controlled band gaps is a critical requirement. Several methods have been introduced to create GNR, one of which is electron beam lithography (Luo and Yu, 2022). In this method, the electron beam rotates on the sample (which is kept under the electrode), then an etching mask with a specific pattern forms the GNR structure in the presence of the electron beam. In the next step, the etched area is scraped with oxygen plasma and the remaining photoresist is removed (Han et al., 2007; Liu et al., 2011). Another method of producing graphene nanoribbons is nanoparticle etching (NPE) (Elías, 2010). In this deposition method, exfoliation of graphene, metal ion solution with spin coating, evaporation of water solvent, reduction of metal nanoparticles, and etching with heat. NPE has an outstanding advantage over EBL and plasma etching that it preserves the obvious edge structure of the prepared GNRs, including graphene edges (Jin, 2016).

6. Conclusion

In conclusion, our study investigated the transmission characteristics and field distribution of band-stop filters utilizing the three-dimensional finite difference in the time domain (3D-FDTD) method. The hourglass-shaped graphene band-stop filter demonstrated transmission characteristics, achieving a maximum attenuation of −52.5 dB at the cut-off frequency of 32.3 THz. By varying the bias voltage and chemical potential of graphene by different amounts, we achieved tunability in the band-stop filter, manipulating the surface conductivity of graphene and thereby shifting the central frequency in the range of 28 to 36 terahertz. With its high transmission efficiency, high tunability, and compact dimensions, this proposal emerges as a promising choice for compact integrated optical telecommunication devices.

Impact Statement:

The research paper presents a groundbreaking hourglass-shaped graphene ribbon band-stop filter with significant implications. Achieving a remarkable bandwidth of 1.2 THz and 90% transmission efficiency, this innovation holds promise for revolutionizing integrated optical telecommunications devices. By enabling high tunability and compact dimensions, it addresses a critical challenge in the field and opens avenues for advanced optical technology applications.

Scope Statement:

The research conducted in this paper focuses on the development and characterization of an hourglass-shaped graphene ribbon band-stop filter. The study employs the three-dimensional finite difference time domain (3D-FDTD) method for comprehensive numerical simulations, covering transmission spectra and electromagnetic field distribution. The proposed filter's scope extends to applications in integrated optical telecommunication devices, offering high transmission efficiency and tunability within the terahertz frequency range (28-36 THz).

CRediT authorship contribution statement

Ghader Mohammadi: Investigation, Writing – original draft. **Aliasghar Orouji:** Writing – review & editing, Supervision. **Mohammad**

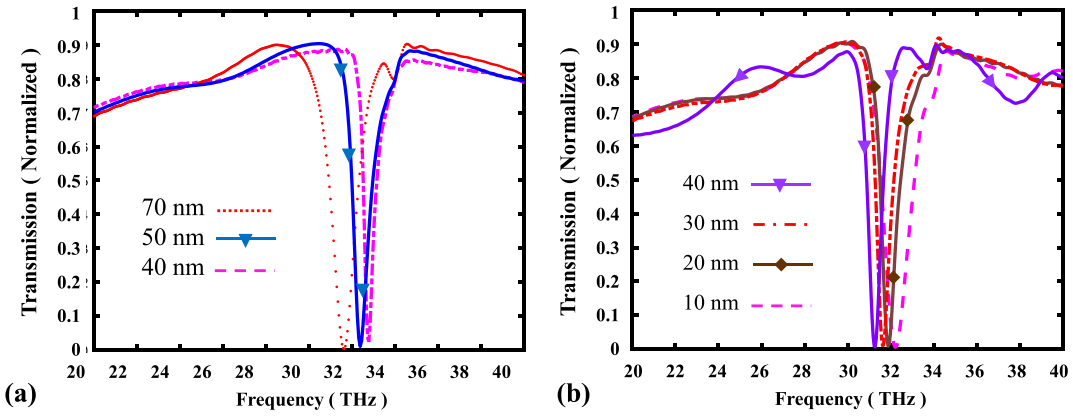

Fig. 6. (a) Transmission spectra for the width of graphene nanoribbons of different sizes (b)Transmission spectrum for the different junctions between the top and bottom of the graphene nanoribbons.

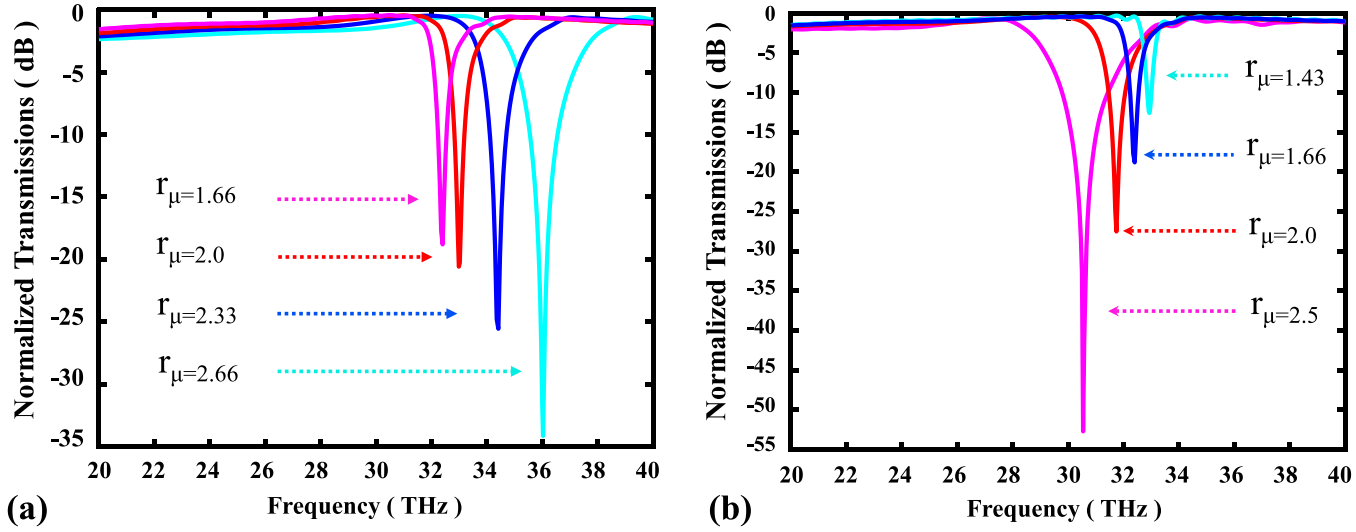

Fig. 7. (a) Displacement of the transmission spectrum in dB with μ_{c1} changes (b) and with μ_{c2} changes.

Table 2
Comparison of the results of the proposed band-stop filter with previously reported papers.

Reference	Year	Structure	Dimensions (nm^2)	BW (THz)	Frequency (THz)	Chemical potential (eV)
(Wei et al., 2016)	2016	graphene	800×800	—	12–22	0.3–0.6
(Shi et al., 2016)	2016	graphene	750×—	3.1	37–53	0.3–0.6
(Cai et al., 2018)	2018	graphene	—	—	12–18	0.3–0.5
(Zhuang et al., 2018)	2018	graphene	—	0.85	15–18	0.145–0.155
(Ze-Jiang and Jiu-Sheng, 2018)	2018	graphene	22500×18000	0.004	5.96–6.01	0.04–0.12
(Abbas and Khaleel, 2019)	2019	graphene	9900×4900	—	7–13	0.1–1
(Naghizade and Saghaei, 2020)	2020	graphene	11500×30000	0.07–0.15	9–25	0.2–0.4
(Karthigeyan et al., 2022)	2022	MIM	75000×75000	0.2–0.8	0.4–2.4	——
(Melo et al., 2022)	2022	graphene	1000×600	7.3	4–12	0.3–0.7
(Li et al., 2022)	2022	graphene-plasmonic	40000×30000	1	1–10	0.2–0.8
(Zonouri and Hayati, 2023)	2023	graphene	500×350	0.72–2.925	2–14	0.3
This paper	2023	graphene	400×300	1.2–2.8	28–36	0.2–0.8

Danaie: Writing – review & editing, Supervision.

Declaration of Competing Interest

The authors declare that they have no known competing financial interests or personal relationships that could have appeared to influence the work reported in this paper.

Data availability

Data will be made available on request.

References

Abbas, M.N., Khaleel, F.A., 2019. Wide-range tunable subwavelength band-stop filter for the far-infrared wavelengths based on single-layer graphene sheet. Ukrainian Journal of Physical Optics 20 (1), 37–45.

Azar, M.T.H., Zavvari, M., Mohammadi, P., Zehforoosh, Y., 2018. Periodically voltage-modulated graphene plasmonic waveguide for band-rejection applications. Journal of Nanophotonics 12 (4), 046002.
Cai, Y., Da Xu, K., Guo, R., Zhu, J., Liu, Q.H., 2018. Graphene-based plasmonic tunable dual-band bandstop filter in the far-infrared region. IEEE Photonics Journal 10 (6), 1–9.
Chashmi, M.J., Rezaei, P., Kiani, N., 2019. Reconfigurable graphene-based V-shaped dipole antenna: From quasi-isotropic to directional radiation pattern. Optik 184, 421–427.
Chashmi, M.J., Rezaei, P., Kiani, N., 2020. Y-shaped graphene-based antenna with switchable circular polarization. Optik 200, 163321.
Chen, P.Y., Argyropoulos, C., Farhat, M., Gomez-Diaz, J.S., 2017. Flatland plasmonics and nanophotonics based on graphene and beyond. Nanophotonics 6 (6), 1239–1262.
Chorsi, H.T., Gedney, S.D., 2016. Tunable plasmonic optoelectronic devices based on graphene metasurfaces. IEEE Photonics Technology Letters 29 (2), 228–230.
Christensen, J., Manjavacas, A., Thongrattanasiri, S., Koppens, F.H., García de Abajo, F. J., 2012a. Graphene plasmon waveguiding and hybridization in individual and paired nanoribbons. ACS Nano 6 (1), 431–440.
Christensen, J., Manjavacas, A., Thongrattanasiri, S., Koppens, F.H., García de Abajo, F.J. J.A.n., 2012b. Graphene Plasmon Waveguiding and Hybridization in Individual and Paired Nanoribbons 6 (1), 431–440.
Danaee, E., Geravand, A., Danaie, M., 2019. Wide-band low cross-talk photonic crystal waveguide intersections using self-collimation phenomenon. Optics Communications 431, 216–228.
Danaie, M., Geravand, A., 2018. Design of low-cross-talk metal–insulator–metal plasmonic waveguide intersections based on proposed cross-shaped resonators. Journal of Nanophotonics 12 (4), 046009.
Danaie, M., Hajshahvaladi, L., Ghaderpanah, E., 2023. A single-mode tunable plasmonic sensor based on an 8-shaped resonator for cancer cell detection. Scientific Reports 13 (1), 13976.
Danielson, E., Sontakke, V.A., Porkovich, A.J., Wang, Z., Kumar, P., Ziadi, Z., Sowwan, M., 2020. Graphene based field-effect transistor biosensors functionalized using gas-phase synthesized gold nanoparticles. Sensors and Actuators B: Chemical 320, 128432.
Elías, A.L., et al., 2010. Longitudinal cutting of pure and doped carbon nanotubes to form graphitic nanoribbons using metal clusters as nanoscalpels. Nano Letters 10 (2), 366–372.
Farbod, M., Laal Dolatabad, Z., Ahangarpour, A., 2022. Fabrication of graphene and N-doped graphene aerogels and comparing their electrical, mechanical, and adsorption capacity properties. Fullerenes, Nanotubes and Carbon Nanostructures 30 (9), 906–912.
Ganguli, A., Faramarzi, V., Mostafa, A., Hwang, M.T., You, S., Bashir, R., 2020. High sensitivity graphene field effect transistor-based detection of DNA amplification. Advanced Functional Materials 30 (28), 2001031.
Gao, Y., Ren, G., Zhu, B., Liu, H., Lian, Y., Jian, S., 2014. Analytical model for plasmon modes in graphene-coated nanowire. Optics express 22 (20), 24322–24331.
Gonçalves, P.A.D., Peres, N.M., 2016. An introduction to graphene plasmonics. World Scientific.
Gosciniak, J., Rasras, M., Khurgin, J.B., 2020. Ultrafast plasmonic graphene photodetector based on the channel photothermoelectric effect. Acs Photonics 7 (2), 488–498.
Gómez-Díaz, J.-S., Perruisseau-Carrier, J., 2013. Graphene-based plasmonic switches at near infrared frequencies. Optics Express 21 (13), 15490–15504.
Hajshahvaladi, L., Kaatuzian, H., Danaie, M., 2022a. A high-sensitivity refractive index biosensor based on Si nanorings coupled to plasmonic nanohole arrays for glucose detection in water solution. Optics Communications 502, 127421.
Hajshahvaladi, L., Kaatuzian, H., Moghaddasi, M., Danaie, M., 2022b. Hybridization of surface plasmons and photonic crystal resonators for high-sensitivity and high-resolution sensing applications. Scientific Reports 12 (1), 21292.
Han, M.Y., Özyilmaz, B., Zhang, Y., Kim, P., 2007. Energy band-gap engineering of graphene nanoribbons. Physical Review Letters 98 (20), 206805.
Heydari, M.B., 2022. Tunable SPPs in graphene-based cylindrical structures with gyroelectric layers. Optik 254, 168651.
Hu, X., Wang, J., 2017. High figure of merit graphene modulator based on long-range hybrid plasmonic slot waveguide. IEEE Journal of Quantum Electronics 53 (3), 1–8.
Hu, Z.-Y., Xia, C.-J., Tang, X.-J., Zhang, T.-T., Yu, J., Liu, Y., 2021. Switching behavior induced by the orientation in triangular graphene molecular junction with graphene nanoribbons electrodes. Optik 225, 165710.
Huang, W., He, N., Ning, R., Chen, Z., 2022. Dual tunable angle filters on graphene and liquid crystal metamatial. Physica E: Low-dimensional Systems and Nanostructures 137, 114995.
Jafari, D., Danaie, M., Orouji, A.A., 2021. Ultra-fast two-bit all-optical analog to digital convertor based on surface plasmons and kerr-type nonlinear cavity. Plasmonics 16 (6), 2101–2108.
Janfaza, M., Mansouri-Birjandi, M.A., Tavousi, A., 2019. Proposal for a graphene nanoribbon assisted mid-infrared band-stop/band-pass filter based on Bragg gratings. Optics Communications 440, 75–82.
Jin, J.E., et al., 2016. Catalytic etching of monolayer graphene at low temperature via carbon oxidation. Physical Chemistry Chemical Physics 18 (1), 101–109.
Karthigeyan, K.A., Radha, S., Manikandan, E., 2022. Polarisation-insensitive and broadband band-stop metamaterial filter for THz waves. Pramana 96 (2), 65.
Khani, S., Danaie, M., Rezaei, P., 2020a. Compact and low-power all-optical surface plasmon switches with isolated pump and data waveguides and a rectangular cavity containing nano-silver strips. Superlattices and Microstructures 141, 106481.
Khani, S., Danaie, M., Rezaei, P., 2020b. All-optical plasmonic switches based on asymmetric directional couplers incorporating Bragg gratings. Plasmonics 15, 869–879.
Khani, S., Farmani, A., Mir, A., 2021. Reconfigurable and scalable 2, 4-and 6-channel plasmonics demultiplexer utilizing symmetrical rectangular resonators containing silver nano-rod defects with FDTD method. Scientific Reports 11 (1), 13628.
Korani, N., Abbasi, A., Danaie, M., 2023. Band-pass and Band-stop Plasmonic Filters Based on Wilkinson Power Divider Structure. Plasmonics 1–10.
Krishnamoorthy, R., Soubache, I., Farmani, A., 2022. Exploring surface plasmon resonance ring resonator structure for high sensitivity and ultra-high-Q optical filter with FDTD method. Optical and Quantum Electronics 54, 1–13.
Kuscu, M., Ramezani, H., Dinc, E., Akhavan, S., Akan, O.B., 2021. Fabrication and microfluidic analysis of graphene-based molecular communication receiver for Internet of Nano Things (IoNT). Scientific Reports 11 (1), 19600.
Li, H.-J., Wang, L.-L., Liu, J.-Q., Huang, Z.-R., Sun, B., Zhai, X., 2013. Investigation of the graphene based planar plasmonic filters. Applied Physics Letters 103 (21).
Li, H.J., Wang, L.L., Sun, B., Huang, Z.R., Zhai, X., 2014. Tunable mid-infrared plasmonic band-pass filter based on a single graphene sheet with cavities. Journal of Applied Physics 116 (22).
Li, H.J., Wang, L.L., Zhang, H., Huang, Z.R., Sun, B., Zhai, X., Wen, S.C., 2014. Graphene-based mid-infrared, tunable, electrically controlled plasmonic filter. Applied Physics Express 7 (2), 024301.
Li, H.J., Wang, L.L., Sun, B., Huang, Z.R., Zhai, X., 2016. Gate-tunable mid-infrared plasmonic planar band-stop filters based on a monolayer graphene. Plasmonics 11, 87–93.
Li, M., Shi, Y., Liu, X., Song, J., Wang, X., Yang, F., 2022. Tunable plasmon-induced transparency in graphene-based plasmonic waveguide for terahertz band-stop filters. Journal of Optics 24 (6), 065002.
Liu, L., Zhang, Y., Wang, W., Gu, C., Bai, X., Wang, E., 2011. Nanosphere Lithography for the Fabrication of Ultranarrow Graphene Nanoribbons and On-Chip Bandgap Tuning of Graphene. Advanced Materials 23 (10), 1246–1251.
Liu, J., Li, P., Chen, Y., Song, X., Mao, Q., Wu, Y., Zhang, W., 2016. Flexible terahertz modulator based on coplanar-gate graphene field-effect transistor structure. Optics Letters 41 (4), 816–819.
Liu, T., Yi, Z., Xiao, S., 2017. Active control of near-field coupling in a terahertz metal-graphene metamaterial. IEEE Photonics Technology Letters 29 (22), 1998–2001.
Luo, H., Yu, G., 2022. Preparation, bandgap engineering, and performance control of graphene nanoribbons. Chemistry of Materials 34 (8), 3588–3615.
Mansouri, M., Mir, A., Farmani, A., 2023. Proposal of a PIT-based pressure sensor using high pairing of MoS2 monolayer and graphene. Optik 278, 170662.
Melo, G., Castro, W., Oliveira, C., 2022. Tunable plasmonic band stop filter based in graphene nanoribbon. Optik 261, 169100.
Mohsin, M., Schall, D., Otto, M., Chmielak, B., Suckow, S., Neumaier, D., 2016. Towards the predicted high performance of waveguide integrated electro-refractive phase modulators based on graphene. IEEE Photonics Journal 9 (1), 1–7.
Moradi, M., Danaie, M., Orouji, A.A., 2022. All-optical NOR and NOT logic gates based on ring resonator-based plasmonic nanostructures. Optik 258, 168905.
Naghdehforushha, S.A., Moradi, G., 2019. High radiation efficiency of coupled plasmonic graphene-based THz patch antenna utilizing strip slot ground plane removal. Optik 182, 1082–1087.
Naghizade, S., Saghaei, H., 2020. Tunable graphene-on-insulator band-stop filter at the mid-infrared region. Optical and Quantum Electronics 52, 1–13.
Nickpay, M.R., Danaie, M., Shahzadi, A., 2022. Graphene-based metamaterial absorber for refractive index sensing applications in terahertz band. Diamond and Related Materials 130, 109539.
Nickpay, M.R., Danaie, M., Shahzadi, A., 2023a. Graphene-based tunable quad-band fan-shaped split-ring metamaterial absorber and refractive index sensor for THz spectrum. Micro and Nanostructures 173, 207473.
Nickpay, M.R., Danaie, M., Shahzadi, A., 2023b. A triple-band metamaterial graphene-based absorber using rotated split-ring resonators for THz biomedical sensing. Optical and Quantum Electronics 55 (2), 193.
Nikitin, A.Y., Guinea, F., García-Vidal, F., Martín-Moreno, L., 2011. Edge and waveguide terahertz surface plasmon modes in graphene microribbons. Physical Review B 84 (16), 161407.
Nohoji, A.H.A., Danaie, M., 2022. Highly sensitive refractive index sensor based on photonic crystal ring resonators nested in a Mach-Zehnder interferometer. Optical and Quantum Electronics 54 (9), 574.
Nouman, M.T., Kim, H.W., Woo, J.M., Hwang, J.H., Kim, D., Jang, J.H., 2016. Terahertz modulator based on metamaterials integrated with metal-semiconductor-metal varactors. Scientific reports 6 (1), 26452.
Romagnoli, M., et al., 2018. Graphene-based integrated photonics for next-generation datacom and telecom. Nature Reviews Materials 3 (10), 392–414.
Ryzhii, V., Ryzhii, M., Mitin, V., Shur, M.S., Otsuji, T., 2020. Far-infrared photodetectors based on graphene/black-AsP heterostructures. Optics Express 28 (2), 2480–2498.
Sepahvandi, V., Rezaei, B., Aly, A., 2023. Tunable multichannel Fibonacci one-dimensional terahertz photonic crystal filter. Scientific Reports 13 (1), 5631.
Shafagh, S.G., Kaatuzian, H., Danaie, M., 2021. Ahighly sensitive tunable filter using hybrid 1-D photonic crystal and plasmonic MIM waveguide. Optik 228, 166174.
Shi, B., Cai, W., Zhang, X., Xiang, Y., Zhan, Y., Geng, J., Ren, M., Xu, J., 2016. Tunable band-stop filters for graphene plasmons based on periodically modulated graphene. Scientific reports 6 (1), 26796.
Shiramin, L.A., Van Thourhout, D., 2016. Graphene modulators and switches integrated on silicon and silicon nitride waveguide. IEEE Journal of Selected Topics in Quantum Electronics 23 (1), 94–100.

Snapp, P., Kang, P., Leem, J., Nam, S., 2019. Colloidal photonic crystal strain sensor integrated with deformable graphene phototransducer. Advanced Functional Materials 29 (33), 1902216.
Tavana, S., Zarifkar, A., Miri, M., 2022. Tunable terahertz perfect absorber and polarizer based on one-dimensional anisotropic graphene photonic crystal. IEEE Photonics Journal 14 (3), 1–9.
Vertuccio, L., De Santis, F., Pantani, R., Lafdi, K., Guadagno, L., 2019. Effective de-icing skin using graphene-based flexible heater. Composites Part B: Engineering 162, 600–610.
Wang, B., Zhang, X., Yuan, X., Teng, J., 2012. Optical coupling of surface plasmons between graphene sheets. Applied Physics Letters 100 (13).
Wang, Xianjun, Meng, Hongyun, Liu, Shuai, Deng, Shuying, Tao Jiao, Zhongchao Wei, Wang, Faqiang, Tan, Chunhua, Xuguang, Huang, 2018. Tunable graphene-based mid-infrared plasmonic multispectral and narrow band-stop filter. Materials Research Express 5 (4), 045804.
Wei, Zhongchao, Li, Xianping, Yin, Jianjun, Huang, Rong, Liu, Yuebo, Wang, Wei, Liu, Hongzhan, Meng, Hongyun, Ruisheng, Liang, 2016. Active plasmonic band-stop filters based on graphene metamaterial at THz wavelengths. Optics Express 24 (13), 14344–14351.
Xiang, Y., Dai, X., Guo, J., Zhang, H., Wen, S., Tang, D., 2014. Critical coupling with graphene-based hyperbolic metamaterials. Scientific Reports 4 (1), 5483.
Xiao, S., Wang, T., Jiang, X., Yan, X., Cheng, L., Wang, B., Xu, C., 2017. Strong interaction between graphene layer and Fano resonance in terahertz metamaterials. Journal of Physics D: Applied Physics 50 (19), 195101.
Xiao, S., Wang, T., Liu, T., Yan, X., Li, Z., Xu, C., 2018. Active modulation of electromagnetically induced transparency analogue in terahertz hybrid metal-graphene metamaterials. Carbon 126, 271–278.
Xing, P., Ooi, K.J., Tan, D.T., 2018. Ultra-broadband and compact graphene-on-silicon integrated waveguide mode filters. Scientific Reports 8 (1), 9874.
Yao, B., et al., 2013. Demonstration of complex refractive index of graphene waveguide by microfiber-based Mach-Zehnder interferometer. Optics Express 21 (24), 29818–29826.
Youngblood, N., Anugrah, Y., Ma, R., Koester, S.J., Li, M., 2014. Multifunctional graphene optical modulator and photodetector integrated on silicon waveguides. Nano letters 14 (5), 2741–2746.
Yousefi, S., Maleki, M., 2023. Plasmonic Perfect Absorber Based on Graphene and Its Sensing Application. Plasmonics 1–10.
Ze-Jiang, Z., Jiu-Sheng, L., 2018. Terahertz band-stop filter based on graphene cavity. Micro & Nano Letters 13 (3), 374–377.
Zhai, D., Zhao, R., Geng, Z., Cui, B., Yang, Y., 2018. A high-selectivity THz band-stop filter based on a flexible polyimide film. In: Infrared, Millimeter-Wave, and Terahertz Technologies V, vol. 10826. SPIE, pp. 189–195.
Zhao, Y., Chen, G., Tao, Z., Zhang, C., Zhu, Y., 2014. High Q-factor plasmonic resonators in continuous graphene excited by insulator-covered silicon gratings. RSC advances 4 (50), 26535–26542.
Zhou, Z., Song, Z., 2022. Terahertz mode switching of spin reflection and vortex beams based on graphene metasurfaces. Optics & Laser Technology 153, 108278.
Zhuang, H., Sheng, S., Kong, F., Li, K., Wang, Y., 2016. A wavelength demultiplexing structure based on graphene nanoribbon resonators. Optics Communications 381, 396–402.
Zhuang, H., Xu, H., Kong, F., Wang, Y., Gao, M., Li, K., 2018. Tunable slow light based on detuned coupling between graphene nanoribbon and square ring splitting modes. Optical and Quantum Electronics 50, 1–10.
Zonouri, S.A., Hayati, M., 2023. A compact graphene-based dual-band band-stop filter using new hook-shaped resonator for THz applications. Materials Science in Semiconductor Processing 153, 107150.